Draft version September 21, 2016
Preprint typeset using LaTeX style emulateapj v. 5/2/11

arXiv:1606.02299v3 [astro-ph.EP] 20 Sep 2016

GAP OPENING IN 3D: SINGLE PLANET GAPS

Jeffrey Fung[1] & Eugene Chiang
Department of Astronomy, University of California at Berkeley, Campbell Hall, Berkeley, CA 94720-3411
Draft version September 21, 2016

ABSTRACT

Giant planets can clear deep gaps when embedded in 2D (razor-thin) viscous circumstellar disks. We show by direct simulation that giant planets are just as capable of carving out gaps in 3D. Surface density maps are similar between 2D and 3D, even in detail. In particular, the scaling $\Sigma_{\rm gap} \propto q^{-2}$ of gap surface density with planet mass, derived from a global "zero-dimensional" balance of Lindblad and viscous torques, applies equally well to results obtained at higher dimensions. Our 3D simulations reveal extensive, near-sonic, meridional flows both inside and outside the gaps; these large-scale circulations might bear on disk compositional gradients, in dust or other chemical species. At high planet mass, gap edges are mildly Rayleigh unstable and intermittently shed streams of material into the gap — less so in 3D than in 2D.

Subject headings: accretion, accretion disks — methods: numerical — planets and satellites: formation — protoplanetary disks — planet-disk interactions — circumstellar matter — stars: variables: T Tauri, Herbig Ae/Be

1. INTRODUCTION

Giant planets are expected to open gaps in their natal circumstellar disks (for a review, see Kley & Nelson 2012). Gaps and cavities have been observed in "transitional" disks such as LkCa 15 (Kraus & Ireland 2012; Sallum et al. 2015), TW Hya (Debes et al. 2013; Akiyama et al. 2015; Nomura et al. 2016), and HD 169142 (Quanz et al. 2013; Reggiani et al. 2014), in addition to the young protoplanetary disk HL Tau (ALMA Partnership et al. 2015). Whether we can say with confidence that these gaps are planetary in origin relies on our understanding of the gap-opening mechanism.

Theoretical studies supported by numerical simulations have investigated how the depths and widths of planetary gaps relate to planet and disk properties (Crida et al. 2006; Duffell & MacFadyen 2013; Fung et al. 2014; Kanagawa et al. 2015, 2016). It has been established from 2D numerical simulations that the surface density within the gap, $\Sigma_{\rm gap}$, follows a power-law scaling relation with planet mass, disk aspect ratio, and disk viscosity. This relation can be derived from a simple "zero-dimensional" (0D) model, where the planet's global disk-integrated Lindblad torque balances the disk viscous torque (Fung et al. 2014, hereafter FSC14; Kanagawa et al. 2015; Duffell & Dong 2015). Whether these results carry over to a realistic 3D disk is not obvious. The Lindblad torque is most strongly exerted in the disk midplane where the planet resides, while the viscous torque applies throughout the disk. Kley et al. (2001) and Bate et al. (2003) reported good agreement between 2D and 3D simulations for a restrictive set of parameters and simulation times (see their Figures 7 and 2, respectively).[2] Morbidelli et al. (2014; see also Szulágyi et al. 2014) reported a meridional circulation inside a planetary gap in their 3D simulations.

Because of the difference in dimensionality, 3D flow patterns cannot be derived from 2D. Flow dynamics specific to 3D can affect disk and planet evolution. For instance, 3D effects may modify the amount of gas that flows around the planet and across the gap, affecting how the planet accretes mass (e.g., Ormel et al. 2015) and migrates (e.g., Benítez-Llambay et al. 2015). Also, 3D flow patterns around gap edges may impact dust filtration and trapping at gap edges, processes so far studied mainly in 2D (e.g., Paardekooper & Mellema 2006; Rice et al. 2006; Zhu et al. 2012).

A technical challenge with 3D planetary gap studies is the long computational timescale involved. As shown by FSC14, the time it takes for a gap to come to steady state scales with the disk viscous time, and can be as long as $\sim 10^4$ planetary orbits when α, the Shakura-Sunyaev viscosity parameter (Shakura & Sunyaev 1973), is 0.001. This long time, together with the generally more costly nature of 3D simulations, has made it difficult to simulate 3D gaps. Fortunately, these obstacles are gradually being removed by technological advances. In this paper, we perform a systematic parameter space study that reveals the steady-state density and flow structure of 3D gaps, which we will compare to 2D results.

Section 2 details our numerical method and simulation parameters. Section 3.1 compares 3D gap results with their 2D counterparts. Section 3.2 details the 3D flow field around gaps, and Section 3.3 investigates the origin of gap unsteadiness. Section 4 concludes and discusses future work.

2. NUMERICAL METHOD

We use the graphics processing unit (GPU) accelerated hydrodynamics code `PEnGUIn` (Fung 2015) to simulate planetary gaps. It is a 3D Lagrangian-remap shock-capturing code that uses the piecewise parabolic method (Colella & Woodward 1984). A 2D version of this code was used by FSC14. A 3D version was implemented by Fung et al. (2015) to simulate the flow field around a low-mass planet, using a setup similar to the one employed here. In this section, we recapitulate some of the main features of `PEnGUIn`, which we will run in both 2D and 3D.

Denoting by $\{r, \phi, \theta\}$ the radial, azimuthal, and polar coordinates, and $R = r \sin\theta$ the cylindrical radius, we write the Lagrangian continuity and momentum equations solved by

email: jeffrey.fung@berkeley.edu

[1] NSERC Fellow

[2] These papers and others of that era argue that gaps open when a planet's Hill sphere radius exceeds the disk's scale height. This criterion is incorrect; even low-mass planets can open gaps, depending on the disk viscosity (Duffell & MacFadyen 2013; FSC14; Kanagawa et al. 2015; Kanagawa et al. 2016; see also Goldreich & Tremaine 1980, their equation 103).

PEnGUIn as:

$$\frac{D\rho}{Dt} = -\rho\left(\nabla\cdot\mathbf{v}\right), \tag{1}$$

$$\frac{D\mathbf{v}}{Dt} = -\frac{1}{\rho}\nabla p + \frac{1}{\rho}\nabla\cdot\mathbb{T} - \nabla\Phi, \tag{2}$$

where ρ is the gas density, $\mathbf{v}$ the velocity field, p the gas pressure, $\mathbb{T}$ the Newtonian stress tensor, and Φ the combined gravitational potential of the star and the planet. The simulations are performed in the corotating frame of the planet, with the Coriolis force absorbed into the conservative form of Equation 2 as suggested by Kley (1998). We adopt a locally isothermal equation of state, such that $p = c^2\rho$, where c is the specified sound speed of the gas. The stress tensor $\mathbb{T}$ is proportional to the kinematic viscosity ν, which we parameterize using the α-prescription of Shakura & Sunyaev (1973), such that $\nu = \alpha c h$, where h is the disk scale height. We fix $\alpha = 0.001$.

The simulations are performed in a frame centered on the star, so for a planet on a fixed, circular orbit in the disk midplane, Φ equals:

$$\Phi = -\frac{GM}{1+q}\left[\frac{1}{r} + \frac{q}{\sqrt{r^2 + R_\mathrm{p}^2 - 2RR_\mathrm{p}\cos\phi' + r_\mathrm{s}^2}} - \frac{qR\cos\phi'}{R_\mathrm{p}^2}\right], \tag{3}$$

where G is the gravitational constant, $M = M_* + M_\mathrm{p}$ the total mass of the star and the planet, $q = M_\mathrm{p}/M_*$ the planet-to-star mass ratio, R_p the semi-major axis of the planet's orbit, r_s the smoothing length of the planet's potential, and $\phi' = \phi - \phi_\mathrm{p}$ denotes the azimuthal separation from the planet. We set $GM = 1$ and $R_\mathrm{p} = 1$, so that the Keplerian velocity and frequency $v_\mathrm{k} = \sqrt{GM/r}$ and $\Omega_\mathrm{k} = \sqrt{GM/r^3}$ both equal 1 at the planet's orbit. We also define Ω_p as the planet's orbital frequency. The third term in the bracket is the indirect potential. The 2D version of Equation 3 is obtained by substituting the spherical r with the cylindrical R. Note that Equation 3 technically differs from the potential used in FSC14, as PEnGUIn simulations in FSC14 were performed in the barycentric frame. This difference in reference frame should not have a significant effect on our results, as was already tested by FSC14.

One qualitative difference between 2D and 3D setups is in the smoothing length r_s. In 2D, r_s is chosen to mimic the vertically averaged gravitational force of the planet, and therefore the appropriate choice should be of order the thickness of the disk, $h = c/\Omega_\mathrm{k}$ (Müller et al. 2012). In 3D, r_s should be set to a value sufficiently small to not interfere with the large-scale gap dynamics of interest here (in contradistinction to the smaller-scale circumplanetary flow). Based on these considerations, we set $r_\mathrm{s} = 0.5\ h_0$ in our 2D simulations, where h_0 is the disk scale height evaluated at the planet's location, and $r_\mathrm{s} = 0.1\ r_\mathrm{H}$ in 3D, where $r_\mathrm{H} = (q/3)^{1/3}R_\mathrm{p}$ is the planet's Hill radius.

2.1. *Initial and boundary conditions*

The initial disk profile assumes the following surface density and sound speed profiles:

$$\Sigma = \Sigma_0\left(\frac{R}{R_\mathrm{p}}\right)^{-\frac{1}{2}}, \tag{4}$$

$$c = c_0\left(\frac{R}{R_\mathrm{p}}\right)^{-\frac{1}{2}}, \tag{5}$$

where we set $\Sigma_0 = 1$,[3] and choose $c_0 = 0.05$. The disk scale height h is therefore $c/\Omega_\mathrm{k} = 0.05R$ with Ω_k evaluated at the midplane; in other words, the disk aspect ratio $h/R = 0.05$ is constant. This sound speed profile is fixed in time, corresponding to an irradiated disk that has a cooling time much shorter than the dynamical time. In 3D hydrostatic equilibrium, the initial density structure is:

$$\rho = \rho_0\left(\frac{R}{R_\mathrm{p}}\right)^{-\frac{3}{2}}\exp\left(\frac{GM}{c^2}\left[\frac{1}{r} - \frac{1}{R}\right]\right), \tag{6}$$

where $\rho_0 = \Sigma_0/\sqrt{2\pi h_0^2}$ is the initial gas density at the location of the planet.

The initial velocity field assumes hydrostatic equilibrium, taking into account gas pressure but not viscosity. As a result, the initial disk has an orbital frequency of

$$\Omega = \sqrt{\Omega_\mathrm{k}^2 + \frac{1}{r}\frac{\partial p}{\partial r}} \tag{7}$$

and zero radial and polar velocity. Given our isothermal equation of state and sound speed profile, our disk model is subject to the vertical shear instability (e.g., Urpin & Brandenburg 1998; Lin & Youdin 2015). However, our disk viscosity of $\nu = 2.5\times10^{-6}$ is sufficient to prevent the instability from growing, as shown by Nelson et al. (2013).

Both the inner and outer radial boundaries are fixed at their initial values. In the polar direction, we simulate only the upper half of the disk to reduce computational cost. We use reflecting boundaries both at the top, to prevent mass from entering or leaving the domain, and at the midplane. Imposing reflection symmetry across the midplane (polar velocity $v_\theta = 0$) means certain dynamics are not captured by our simulation, such as flows that cross the midplane, and bending waves near the midplane. It remains to be determined whether these restrictions affect the results of our study.

2.2. *Resolution*

Our simulation domain extends radially from 0.4 to 2 R_p, and spans the full 2π in azimuth. The polar angle in our 3D simulations spans 0 to 12 degrees, equivalent to a vertical extent of 4 scale heights.

We use 270 logarithmically spaced cells in the radial direction, 810 uniformly spaced cells in the azimuthal direction, and 45 uniformly spaced cells in the polar direction. This resolution translates to about 8, 6, and 11 cells per scale height in each of the $\{r, \phi, \theta\}$ directions, respectively. This choice is motivated by Figure 2 of FSC14.

2.3. *Metrics*

As in FSC14, we define the surface density in the gap, Σ_gap, as a spatial average over the annulus spanning $R = R_\mathrm{p} - \Delta$ to $R_\mathrm{p} + \Delta$ with $\Delta \equiv 2\ r_\mathrm{H}$, excised from $\phi = \phi_\mathrm{p} - \Delta/R_\mathrm{p}$ to $\phi_\mathrm{p} + \Delta/R_\mathrm{p}$. Throughout this paper, we will also show velocity plots and maps that are temporal and/or spatial averages. In all instances, velocities are averages weighted by gas density.

[3] Since we do not consider the self-gravity of the disk, this normalization has no impact on our results.

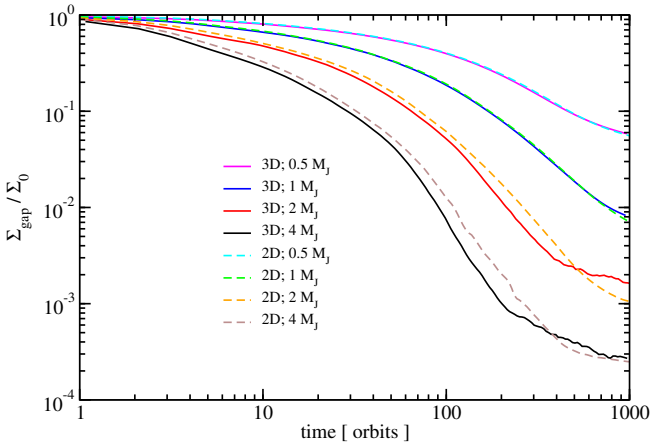

FIG. 1.— Σ_{gap} versus time for all our simulations. Solid (dashed) lines plot our 3D (2D) results. Comparing our 2D results to those of FSC14 (their Table 1 and Figure 5), we find that our measurements of Σ_{gap} have converged to within a factor of 2 of theirs after 1000 orbits. The agreement between our 2D and 3D results is close, particularly for 0.5 M_J and 1 M_J.

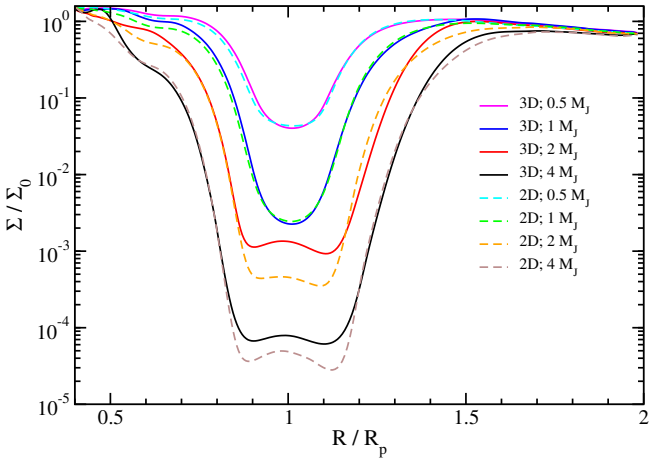

FIG. 2.— Surface density profiles, averaged azimuthally except for a small area around the planet ($\{\phi_p - \Delta/R_p, \phi_p + \Delta/R_p\}$), and averaged in time from 1000 to 1010 planetary orbits. The slight density enhancement at $R = R_p$ when $M_p \geq 2M_J$ is due to gas concentrating about the triangular (i.e., Trojan) Lagrange points.

3. RESULTS

3.1. *Gap depth and shape*

We perform four 3D simulations with q varying between 0.0005 and 0.004 (0.5 to 4 M_J). For our parameters, the planet's Hill radius r_H ranges from 1.1 to 2.2 times the local disk scale height h_0. We also run four 2D simulations using the same parameters for comparison; these are nearly exact replicates of the simulations from FSC14. Figure 1 plots the gap depth contrast Σ_{gap}/Σ_0 versus time for our 2D and 3D simulations. Because of the costly nature of 3D simulations, we were only able to simulate up to 10^3 orbits. By comparison, FSC14 ran up to $\sim 10^4$ orbits to achieve steady state. Comparing our Figure 1 with Figure 5 of FSC14 indicates that our results for Σ_{gap}/Σ_0 have converged to within a factor of 2 of theirs. We consider such convergence sufficient to identify differences between 2D and 3D gaps. Our results show some time variability, particularly for high-mass runs, that we will investigate in Section 3.3.

Figure 1 shows clearly that Σ_{gap} behaves in 3D similarly to how it does at lower dimensionality. In particular, the final values of Σ_{gap} in 3D scale as q^{-2}, as predicted by the 0D models of FSC14 and Kanagawa et al. (2015). The agreement between 2D and 3D simulations is astonishingly close for $M_p \leq M_J$. For $M_p = 2M_J$ and $4M_J$, Σ_{gap} decreases initially more rapidly in 3D than in 2D, but ultimately reaches a slightly larger value (about ~80% larger in the case $M_p = 2M_J$).

For 3D simulations, to verify that our fiducial choice for smoothing length $r_s = 0.1r_H$ is sufficiently small, we perform a test case at $M_p = 4M_J$ with $r_s = 0.05r_H$, and find that Σ_{gap} changes negligibly. For 2D simulations, the correct choice of r_s is less clear; although any value of order h_0 is suitable in principle (Müller et al. 2012), the value of Σ_{gap} is sensitive to r_s. For example, we find that using $r_s = 1\ h_0$ instead of our fiducial 0.5 h_0 results in a ~40% larger Σ_{gap}. In this regard, we should not overinterpret the exceptionally close agreement between 2D and 3D results.

Figure 2 plots the azimuthally averaged surface density profiles, excluding a small $\pm\Delta/R_p$ azimuthal range around the planet. In terms of both gap width and the sharpness of gap edges, the 3D gaps are remarkably similar to 2D gaps. The resemblance is confirmed in face-on views of surface density, as presented in Figure 3. The 2D gaps show more distinct streamers within the gaps. These filaments appear related to the Rayleigh instability operating at gap edges, as we discuss in Section 3.3.

3.2. *3D Flow Topology*

The flow pattern in 3D may be expected to deviate significantly from that in 2D. In 3D, not only are vertical velocities allowed, but radial velocities can be larger since planetary and viscous torques do not have to cancel locally; the former is mostly exerted in the midplane, while the latter can be exerted anywhere.

Figures 4 and 5 illustrate the meridional flow in our $1M_J$ and $4M_J$ simulations. In agreement with the results of Szulágyi et al. (2014) and Morbidelli et al. (2014), we find that within the gap, there exists a radial flow directed away from the planet's orbit near the midplane, and another flow delivering gas back into the gap at higher altitudes (Figure 4). Whereas Morbidelli et al. (2014) describe a closed, localized circulation, where the gas is trapped in a cyclical flow near the gap, the flow pattern that we uncover is less localized. We find vigorous motion outside the gap as well as inside with multiple eddy-like structures (Figure 5).

Figure 6 is a schematic drawing of the overall meridional flow field. Outside the gap, steep density gradients drive a viscous flow into the gap ("gradient-driven" flow shown in red). At the same time, the planet drives a fast, denser midplane flow directed away from the gap ("planet-driven" flow shown in blue). These two flows collide near the gap edges, where more complex flow patterns emerge. Because midplane disk pressure decreases outward, the planet-driven flow encounters little resistance moving beyond the outer gap edge, and is able to reach a radial distance of ~4 r_H away from the planet's orbit before being deflected. By comparison, on the opposite, interior half of the gap, the planet-driven flow is deflected at ~2 r_H because of the higher gas pressure characterizing the inner gap edge. Where the planet-driven flow collides with the gradient-driven flow, the local pressure and density are enhanced. The build-up of pressure at the midplane drives gas upward (the "combined" flow shown in magenta) which eventually falls back down toward the midplane. Meridional eddies are created whose rotation poles point in the $-\phi$ direc-

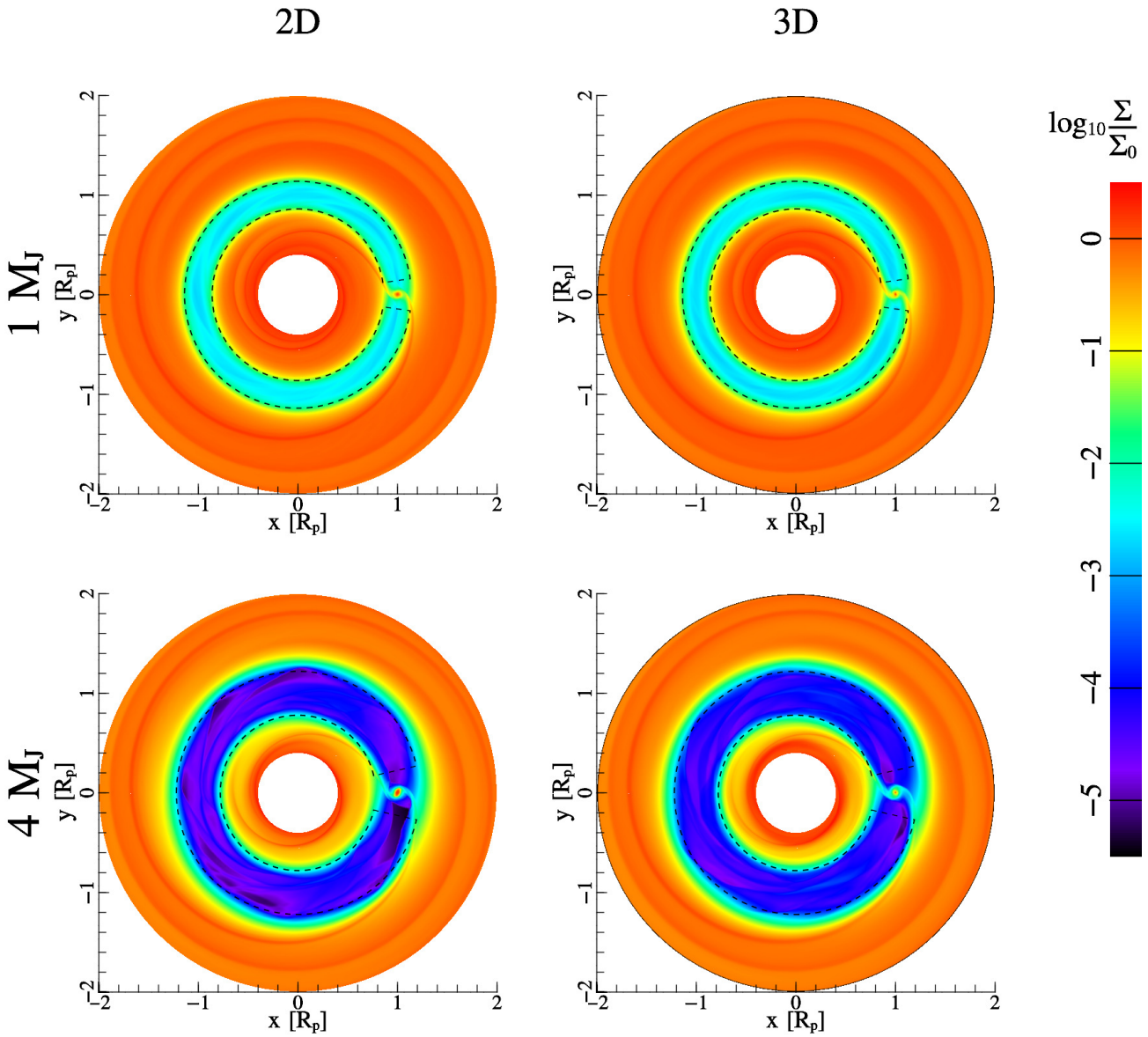

FIG. 3.— Surface density snapshots for our $1M_J$ and $4M_J$ simulations, taken at 1000 planetary orbits. Gaps in 3D (right) and 2D (left) have similar depths and widths. Black solid lines enclose the region where Σ_{gap} is evaluated (see Section 2.3 and Figure 1). Gap streamers are evident in all snapshots, particularly in 2D and for $4M_J$, and are likely caused by the Rayleigh instability at gap edges (see Section 3.3).

tion, just outside either gap edge. The eddies are strongest near the planet and persist downstream for ∼1–2 radians.

The meridional eddies extend as high as our vertical simulation boundaries allow. Gas is carried all the way from the disk midplane to a few scale heights above, and back. This vertical circulation enables the system to reach a near-steady state: the angular momentum acquired by a gas element at low altitude, where the planetary torque dominates, nearly cancels with the angular momentum acquired at high altitude, where the viscous torque dominates. This change in the sign of the net torque is illustrated by the left panel of Figure 7, which shows that the planetary torque, integrated over a portion of the outer disk for the $1M_J$ case, dominates near the midplane, but falls rapidly with altitude and is eventually overtaken by the viscous torque. Note that the precise altitude where this sign change occurs is radially dependent, because the planetary torque is strongest close to the planet, while the viscous torque is strongest near the gap edge. The right panel of Figure 7 plots the angular momentum flux in the polar direction, F_θ, integrated over the same portion of the outer disk:

$$F_\theta = \int_0^{2\pi} \int_{1.1}^{1.8} \langle \rho v_\phi v_\theta r \sin\theta \rangle r \, \mathrm{d}r \, \mathrm{d}\phi \tag{8}$$

where the brackets indicate a time average from 1000 to 1010 orbits. In Figure 7 we separate F_θ into its upward ($v_\theta < 0$) and downward ($v_\theta > 0$) components. The difference between the upward and downward fluxes is small but significant: the net residual is similar in magnitude to the planetary and viscous torques plotted on the left panel of Figure 7. This result is consistent with our interpretation that torque balance is achieved through vertical transport. A more explicit verification of the balance is difficult because the flow varies strongly in time and space, and flow patterns are not strictly closed.

Figure 8 plots the vertically and azimuthally averaged meridional speeds of our 3D simulations. The speeds come

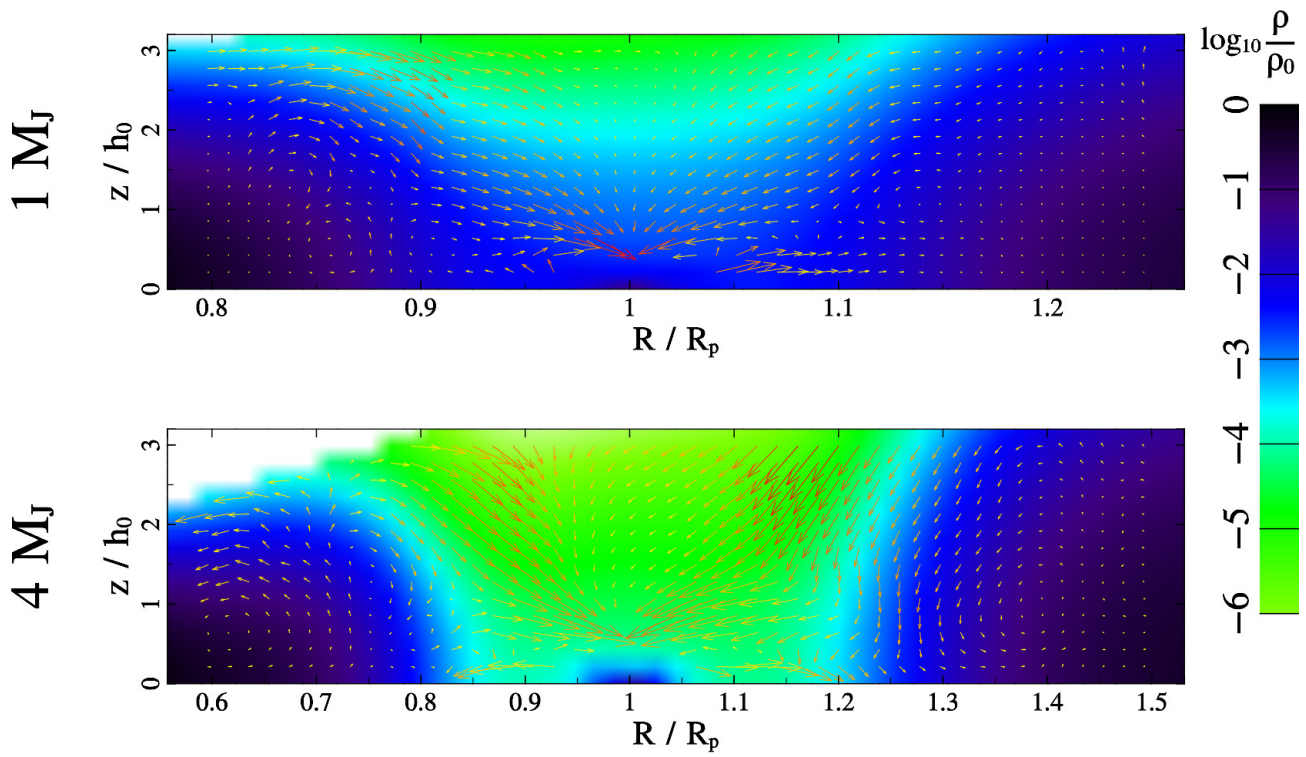

FIG. 4.— Meridional flow fields obtained at the end of our 1 M_J and 4 M_J simulations. Arrows represent velocity vectors, and arrow lengths represent speeds. The longest arrows correspond to 0.2 c_0 for the top panel, and 0.4 c_0 for the bottom. Background color represents gas density. Both density and velocity are azimuthally averaged over the entire 2π, and time averaged from 1000 to 1010 planetary orbits. Velocity vectors within 0.5 r_H of the planet are omitted for clarity. We note that the bottommost row of arrows represent velocities near but not exactly at the midplane. Because of the reflective boundary we impose at the midplane, the polar velocity at $\theta = \pi/2$ (the midplane) is strictly zero.

within an order of magnitude of the sound speed over distances comparable to the planet's orbital radius, and are supersonic closest to the planet (e.g., there is a Mach ~ 5 shock deep inside the $4M_J$ planet's Hill sphere). The planet's influence extends well beyond Hill sphere scales; for example, the most distant principal Lindblad resonances are located at 0.63 R_p in the inner disk (2:1 resonance), and 1.59 R_p in the outer disk (1:2 resonance).

Figure 9 plots 2D maps of the vertical velocity v_z, vertically averaged over the upper half of the disk above the midplane (recall that our simulations assume reflection symmetry about the midplane), and gives a sense of the flow's azimuthal variations. The fastest downward flows in the gap are concentrated within ~1 r_H of the planet. The velocities are comparable to the sound speed, as befits gas that has freely fallen a distance ~ r_H over a timescale Ω^{-1}. Farther away azimuthally, the flow speed reduces by factors of a few and fluctuates spatially and temporally.

Vertical velocities might be used one day to distinguish planet-opened gaps from other kinds of gaps (e.g., Zhang et al. 2015; Béthune et al. 2016), provided velocity signatures above and below the disk midplane along the observer's line of sight do not cancel to zero. A net velocity of zero would be obtained if the disk were exactly reflection-symmetric about the midplane, optically thin in the line used to measure Doppler shifts, and viewed face-on. Rotational transitions from CO may be optically thick, even in the low density environment of a gap. For example, at a temperature of 100 K and a CO/H_2 number abundance of 10^{-4}, the J=4-3 CO line is optically thick at line center down to $\Sigma \sim 10^{-4}$ g/cm^2.

3.3. *Rayleigh instability at gap edges*

Here we offer an explanation for the origin of gap streamers, sometimes called filaments, that have been observed in gap-opening simulations (e.g., de Val-Borro et al. 2006). These streamers arise from unsteady gap edges. In our simulations, they are seen in both 2D and 3D, but more so in 2D, and when $M_p \geq 2M_J$.

The Rayleigh instability can operate at gap edges where the rotation profile is significantly modified by gas pressure gradients. This dynamical instability occurs wherever the specific angular momentum decreases outward:

$$\frac{\partial l}{\partial R} < 0\,, \tag{9}$$

where $l = R^2\Omega$ is the specific angular momentum. Combining this with Equation 7 imposes a condition on the second radial derivative of the gas pressure, and by extension the sharpness of gap edges (e.g., Yang & Menou 2010). Kanagawa et al. (2015) have used this condition to model gap profiles.

Figure 10 plots the azimuthally averaged values of $\partial l/\partial R$ for our 2D and 3D simulations. For 3D, we plot the midplane values. We find that when $M_p \geq 2M_J$ in 2D, or $M_p = 4M_J$ in 3D, the gap edges are Rayleigh unstable. These cases coincide with the appearance of unsteady gap edges and enhanced streamers. We have continued our 2D, $4M_J$ simulation to 10^4 orbits to verify that the gap edges remain unstable even at late times.

There is a slight difference between the 3D and 2D angular momentum profiles, in that the former violates the Rayleigh criterion to a lesser degree. Coinciding with this difference

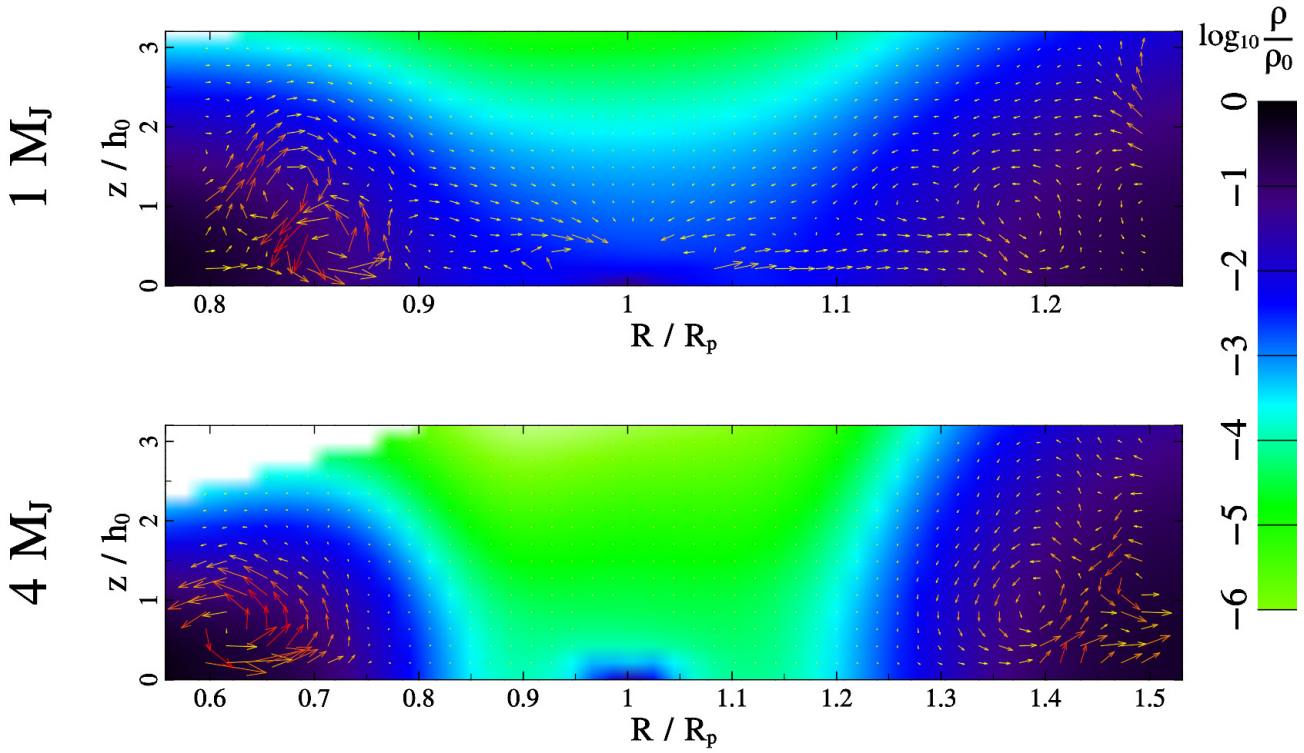

FIG. 5.— Similar to Figure 4, but with arrows representing meridional momentum (averaged over azimuth and time; the longest arrows correspond to 0.0014 $\rho_0 c_0$ for the top panel, and 0.0073 $\rho_0 c_0$ for the bottom). Plotting the momentum highlights the eddies just outside the gap edges; plotting the velocity as in Figure 4 highlights the flow inside the gap.

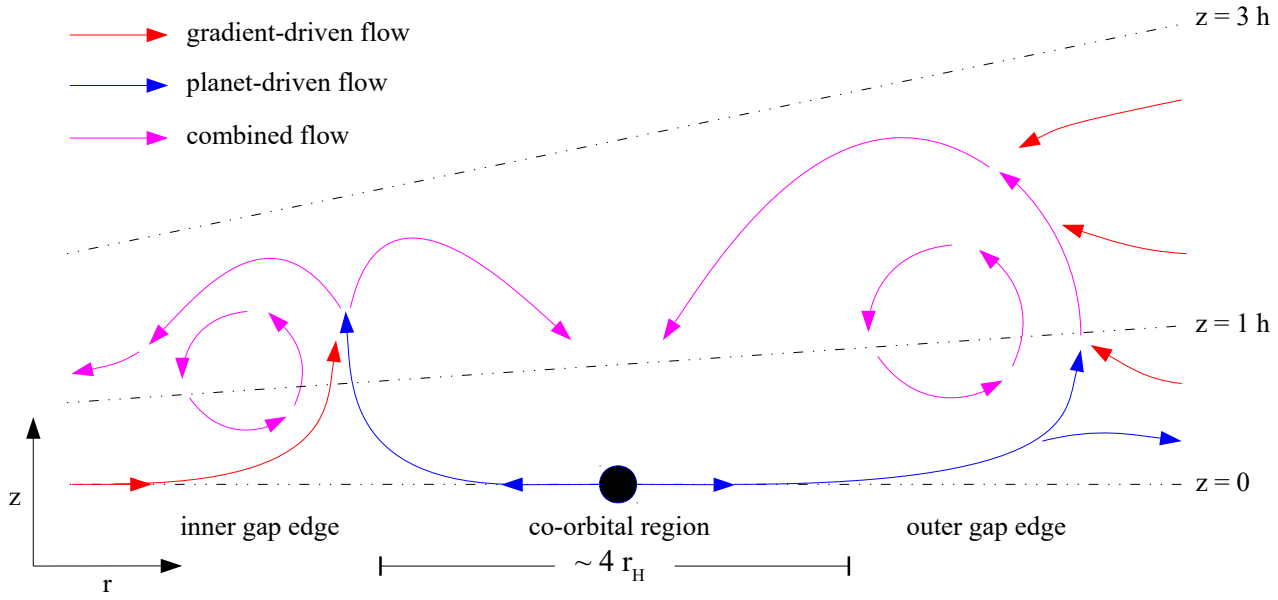

FIG. 6.— A simplified schematic of the meridional flow field, abstracted from Figures 4 and 5. The "planet-driven flow" (represented by blue arrows) is generated by the planet's repulsive Lindblad torques. The "gradient-driven flow" (red arrows) is driven by viscous torques acting to diffuse material from the gap edges into the gap. The collision of these two flows near the midplane increases the density and pressure there relative to vertical hydrostatic equilibrium, forcing the merged flow (magenta arrows) upward and driving a meridional circulation. The eddies at gap edges are strongest near the planet and persist downstream of its location for ~1–2 rad in azimuth.

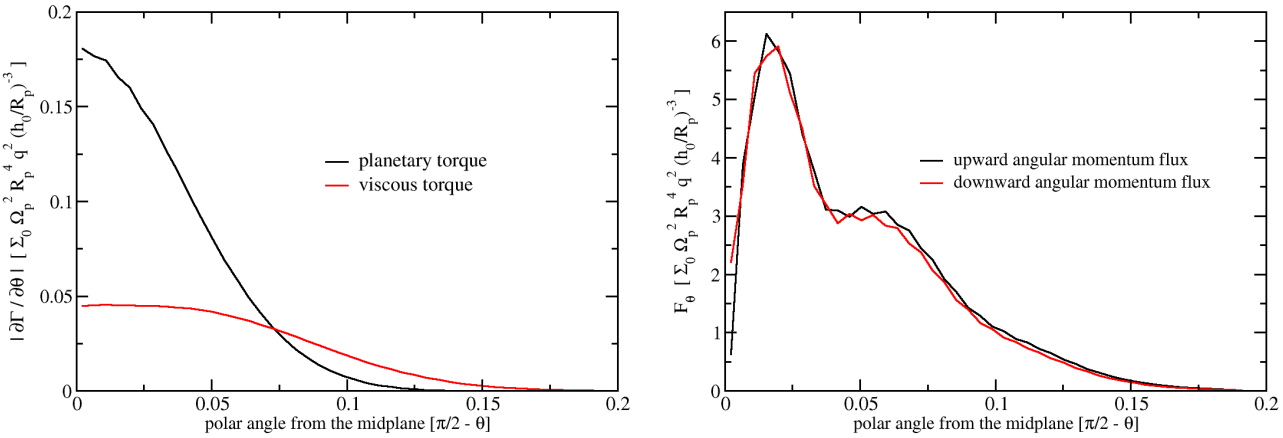

FIG. 7.— Left: absolute values of the planetary (black) and viscous (red) torques, differentiated along the polar angle. Right: angular momentum flux in the polar direction, with the upward (away from the midplane) component plotted in black, and the downward (toward the midplane) component in red. The values are obtained from the $1M_J$ simulation, integrated radially from r = 1.1 to 1.8 and azimuthally over 2π, and time averaged from 1000 to 1010 orbits. The torque exerted on the disk by the planet is positive, while the viscous torque is negative. The left panel shows that at higher altitudes, the viscous torque overtakes the planetary torque, changing the sign of the net torque. The right panel shows that at a given altitude (θ), angular momentum is carried both upward (at certain locations in r and ϕ) and downward (at other locations), with the two fluxes in close but not perfect balance — their difference is comparable in magnitude to the planetary and viscous torques plotted on the left, supporting our interpretation that torque balance is achieved by vertical transport.

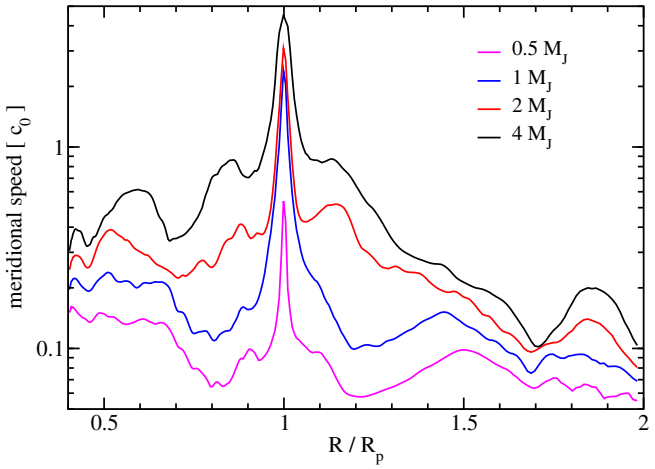

FIG. 8.— Meridional speeds (vertical and radial velocities added in quadrature, and averaged azimuthally and vertically) versus cylindrical radius in our 3D simulations. All profiles are evaluated after 1000 planetary orbits and normalized to c_0, the disk sound speed at the planet's location. Jupiter-mass planets generate near-sonic meridional flows over radial distances comparable to their orbital radii.

— and arguably causally related — is the fact that the streamers leaking into the gap are less prominent in 3D than in 2D (Figure 3). In general, as demonstrated in Figure 11, the 3D torques are somewhat weaker than the 2D torques — by up to ~50% in the case of the $4M_J$ run. We note that this implies that a larger smoothing length r_s in 2D may produce a better match to 3D results for higher planet masses.

The Rayleigh instability may limit the extent to which gaps can be emptied. As the explicit disk viscosity decreases, the gap deepens, its edges become more prone to instability, and more streamers leak into the gap (see also Section 4.2 of FSC14). Thus the Rayleigh instability serves to provide an effective viscosity, transporting angular momentum outward to counter the planet's torque and establishing a "floor" on the gap surface density.

4. SUMMARY AND DISCUSSION

Previous work on gap opening by planets has been plagued by the question of whether 2D results carry over to realistic 3D disks. We have concluded from our numerical study that at least some features do. For our model parameters, gaps in 2D and 3D share nearly identical depths and widths. Though this result could not have been predicted without explicit 3D calculations like those we have undertaken, the similarity between 2D and 3D is, in retrospect, sensible. The 2D equations are merely the vertically integrated versions of the 3D equations; in 3D, it must still be true that the planetary and viscous torques, averaged over large enough volumes, balance in steady state, as they do in 2D (modulo the small residual from the global viscous torque that eventually brings the entire disk onto the star). The balance in 3D is not achieved by a static cancellation of forces at every point in space, but through a dynamic equilibrium between meridional flows driven by the planet, and meridional flows driven by viscosity.

To recapitulate our main findings:

1. Gaps carved in 3D by giant planets resemble their 2D counterparts in depth and shape (Figures 1, 2, and 3).

2. Meridional flows are generated by the spatial mismatch between the planet's torque and the disk's viscous torque (Figures 4, 5, and 6). The flows extend vertically up to a few scale heights, and radially over distances comparable to the planet's orbital radius (Figure 8).

3. Velocities near a giant planet's orbit approach and exceed the sound speed. Such fast flows may be used to distinguish planetary gaps from gaps produced by other mechanisms (Figure 9).

4. The steepest gap edges become Rayleigh unstable (Figure 10) and shed streamers that leak into the gap.

There are some caveats regarding our results. First, our viscous disk models may not accurately represent protoplanetary disks, which may instead be turbulent (e.g., Fromang et al. 2011; Shi et al. 2012). Second, limited by computational resources, we have not investigated how our results scale with disk viscosity or temperature. A more thorough parameter space study should be possible as computing technology continues to advance. Third, insofar as accretion by the planet itself could further reduce the ambient gas density, the $\Sigma_{\rm gap}$ values found in this work should be considered upper limits. Lastly, we have assumed midplane symmetry and only simulated the upper half of the disk. The validity of this assumption will need to be tested by future work.

We close by discussing some directions for future work on planet-disk interactions.

4.1. *Planet Accretion*

Disk flows are directed onto the planet above its poles, and away from the planet in the equator plane (Kley et al. 2001; Klahr & Kley 2006; Tanigawa et al. 2012; Szulágyi et al. 2014; Morbidelli et al. 2014; Ormel et al. 2015; Fung et al. 2015). The giant planets simulated here should be in the final "runaway" phase of their mass accretion history, when the self-gravity of their gas envelopes is significant. Accretion rates for planets in this regime, such as those simulated by D'Angelo et al. (2003) and Machida et al. (2010), and calculated analytically by Tanigawa & Tanaka (2016), show a clear dependence on the ambient gas density. The gap depth should therefore matter for planet accretion rates and luminosities. The converse should also be true. To assess the effect of planetary accretion on the gap density, we would need to adopt a different planet boundary condition than our present smoothing length prescription.

4.2. *Meridional Flows*

The large-scale vertical and radial flows induced by giant planets may affect a number of disk processes: the radial transport of grains (see, e.g., Ogliore et al. 2009 for possible implications of the *Stardust* mission); dust filtration at gap edges which can impact the appearance of transitional disks (e.g., Zhu et al. 2014); the ability of dust to settle vertically, which can affect the disk's spectral energy distribution (e.g., Chiang et al. 2001); and disk chemistry (e.g., Bergin et al. 2007; Dutrey et al. 2014).

4.3. *Gap Opening by Multiple Planets*

The wide radial extents of the cavities in transitional disks have led some to invoke gap opening by multiple planets (Zhu et al. 2011). Simulations in 2D of multi-planet gaps have found that common gaps (the merged gaps of more than one planet) have significantly higher gas density than single-planet gaps (Duffell & Dong 2015), making it more difficult to

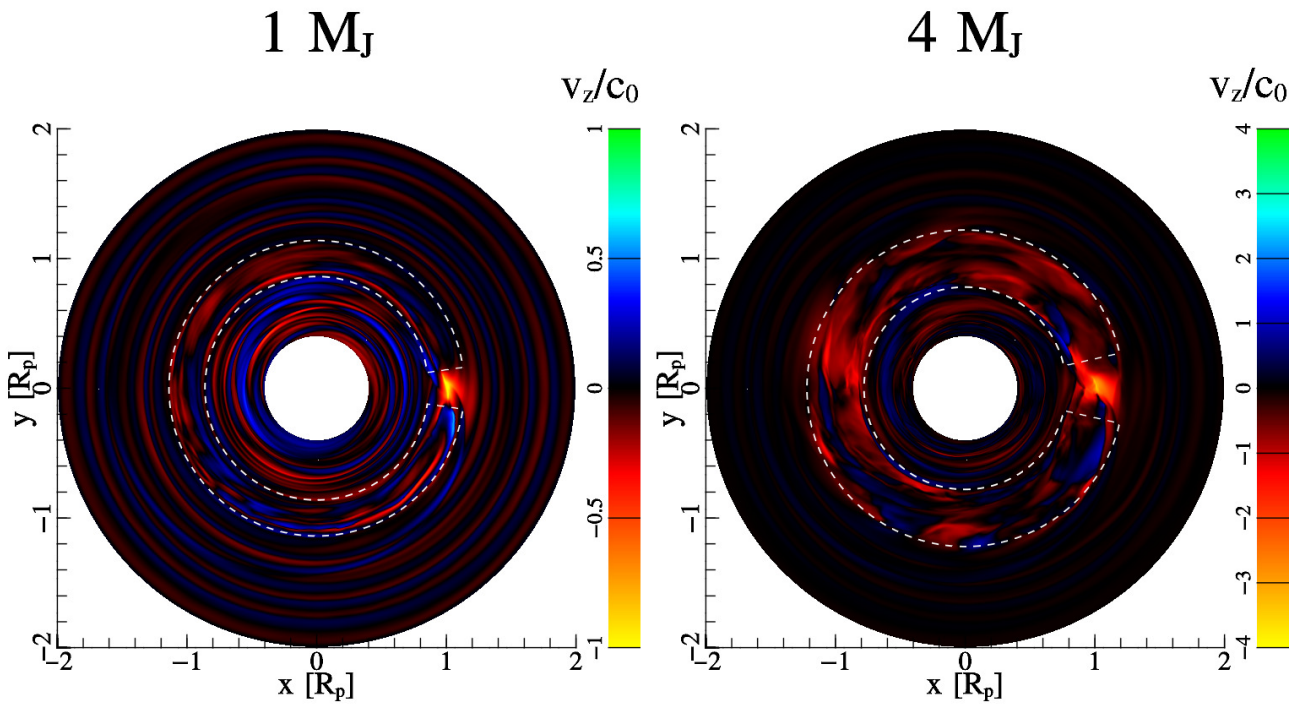

FIG. 9.— Snapshots of the vertically averaged vertical velocity for $1M_J$ (left) and $4M_J$ (right) at 1000 planetary orbits. The vertical average is taken over the upper half of the disk only; this is our entire simulation domain, as we assume the bottom half of the disk is reflection-symmetric about the midplane. The white dashed lines enclose the region where Σ_{gap} is calculated (see Section 2.3 and Figure 1). Blue and green colors represent gas moving with positive vertical velocities (away from the midplane), while red and yellow indicate the opposite. Just above the planet, velocities are supersonic and directed toward it.

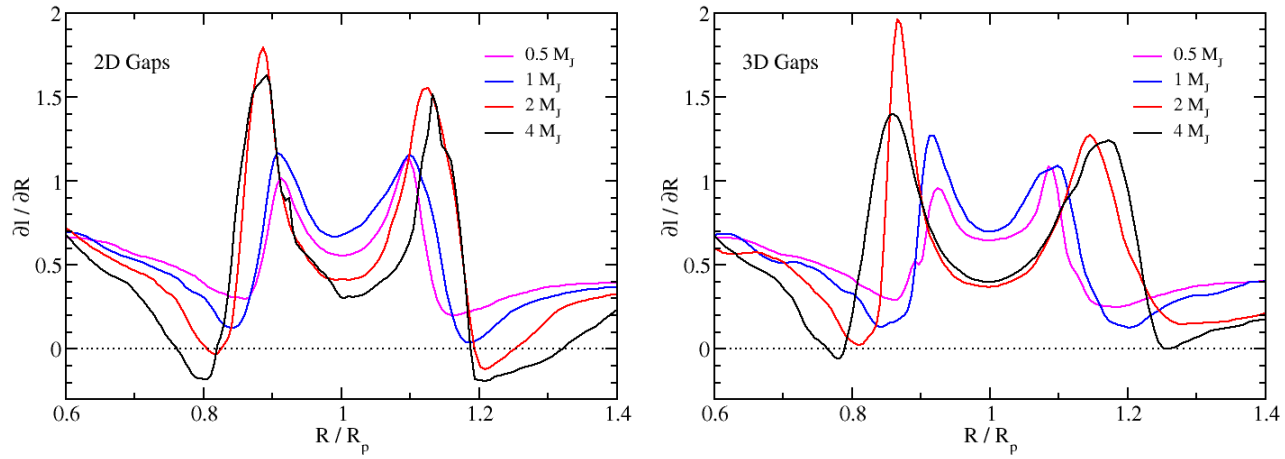

FIG. 10.— Differential angular momentum profiles for all 8 of our simulations, with 2D models on the left and 3D ones on the right. They are azimuthally averaged, excluding the small range around the planet $\phi = \{\phi_p - \Delta/R_p, \phi_p + \Delta/R_p\}$, and obtained at 1000 planetary orbits. For our 3D models, the profiles are taken at the midplane. Where the profile becomes negative is where the disk becomes Rayleigh unstable. The 2D profiles are more unstable than the 3D profiles.

reproduce the transparency of transition disk holes. We plan to test this result in 3D in a forthcoming paper.

We thank Willy Kley, Frédéric Masset, Alessandro Morbidelli, Ji-Ming Shi, and Judit Szulágyi for helpful exchanges. JF gratefully acknowledges support from the Natural Sciences and Engineering Research Council of Canada, and the Center for Integrative Planetary Science at the University of California, Berkeley. EC acknowledges support from grant AST-1411954 awarded by the National Science Foundation, and NASA Origins grant NNX13AI57G.

REFERENCES

Akiyama, E., Muto, T., Kusakabe, N., et al. 2015, ApJL, 802, L17
ALMA Partnership, Brogan, C. L., Pérez, L. M., et al. 2015, ApJL, 808, L3
Bate, M. R., Lubow, S. H., Ogilvie, G. I., & Miller, K. A. 2003, MNRAS, 341, 213
Benítez-Llambay, P., Masset, F., Koenigsberger, G., & Szulágyi, J. 2015, Nature, 520, 63
Bergin, E. A., Aikawa, Y., Blake, G. A., & van Dishoeck, E. F. 2007, Protostars and Planets V, 751
Béthune, W., Lesur, G., & Ferreira, J. 2016, A&A, 589, A87

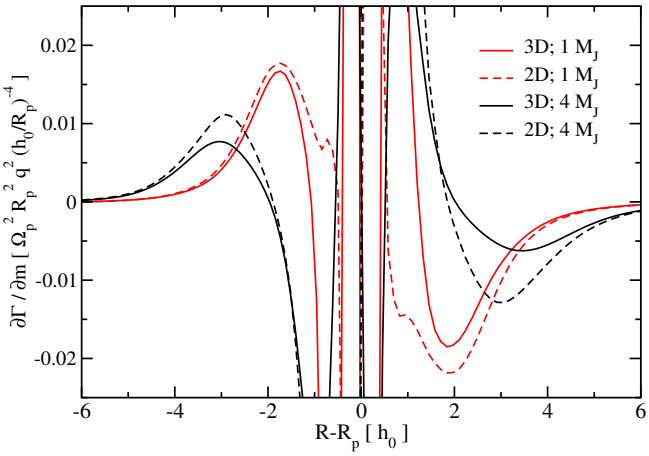

FIG. 11.— Planetary torque density, azimuthally integrated and time averaged from 1000 to 1010 planetary orbits, for our 1 and 4 M_J models. More than $\sim 1\ h_0$ from the planet, the torque profiles show qualitatively good agreement between 2D (dashed) and 3D (solid) calculations, with the 3D torques being systematically weaker. Within $\sim 1\ h_0$, the 2D and 3D profiles differ substantially because of the different smoothing lengths employed (see Section 2).

Chiang, E. I., Joung, M. K., Creech-Eakman, M. J., et al. 2001, ApJ, 547, 1077
Colella, P., & Woodward, P. R. 1984, Journal of Computational Physics, 54, 174
Crida, A., Morbidelli, A., & Masset, F. 2006, Icar, 181, 587
D'Angelo, G., Kley, W., & Henning, T. 2003, ApJ, 586, 540
de Val-Borro, M., Edgar, R. G., Artymowicz, P., et al. 2006, MNRAS, 370, 529
Debes, J. H., Jang-Condell, H., Weinberger, A. J., Roberge, A., & Schneider, G. 2013, ApJ, 771, 45
Duffell, P. C., & Dong, R. 2015, ApJ, 802, 42
Duffell, P. C., & MacFadyen, A. I. 2013, ApJ, 769, 41
Dutrey, A., Semenov, D., Chapillon, E., et al. 2014, Protostars and Planets VI, 317
Fromang, S., Lyra, W., & Masset, F. 2011, A&A, 534, A107
Fung, J. 2015, PhD thesis, University of Toronto, Canada
Fung, J., Artymowicz, P., & Wu, Y. 2015, ApJ, 811, 101
Fung, J., Shi, J.-M., & Chiang, E. 2014, ApJ, 782, 88
Goldreich, P., & Tremaine, S. 1980, ApJ, 241, 425
Kanagawa, K. D., Muto, T., Tanaka, H., et al. 2016, ArXiv e-prints, arXiv:1603.03853
Kanagawa, K. D., Tanaka, H., Muto, T., Tanigawa, T., & Takeuchi, T. 2015, MNRAS, 448, 994
Klahr, H., & Kley, W. 2006, A&A, 445, 747
Kley, W. 1998, A&A, 338, L37
Kley, W., D'Angelo, G., & Henning, T. 2001, ApJ, 547, 457
Kley, W., & Nelson, R. P. 2012, ARA&A, 50, 211
Kraus, A. L., & Ireland, M. J. 2012, ApJ, 745, 5
Lin, M.-K., & Youdin, A. N. 2015, ApJ, 811, 17
Machida, M. N., Kokubo, E., Inutsuka, S.-I., & Matsumoto, T. 2010, MNRAS, 405, 1227
Morbidelli, A., Szulágyi, J., Crida, A., et al. 2014, Icar, 232, 266
Müller, T. W. A., Kley, W., & Meru, F. 2012, A&A, 541, A123
Nelson, R. P., Gressel, O., & Umurhan, O. M. 2013, MNRAS, 435, 2610
Nomura, H., Tsukagoshi, T., Kawabe, R., et al. 2016, ApJL, 819, L7
Ogliore, R. C., Westphal, A. J., Gainsforth, Z., et al. 2009, Meteoritics and Planetary Science, 44, 1675
Ormel, C. W., Shi, J.-M., & Kuiper, R. 2015, MNRAS, 447, 3512
Paardekooper, S.-J., & Mellema, G. 2006, A&A, 453, 1129
Quanz, S. P., Avenhaus, H., Buenzli, E., et al. 2013, ApJL, 766, L2
Reggiani, M., Quanz, S. P., Meyer, M. R., et al. 2014, ApJL, 792, L23
Rice, W. K. M., Armitage, P. J., Wood, K., & Lodato, G. 2006, MNRAS, 373, 1619
Sallum, S., Follette, K. B., Eisner, J. A., et al. 2015, Nature, 527, 342
Shakura, N. I., & Sunyaev, R. A. 1973, A&A, 24, 337
Shi, J.-M., Krolik, J. H., Lubow, S. H., & Hawley, J. F. 2012, ApJ, 749, 118
Szulágyi, J., Morbidelli, A., Crida, A., & Masset, F. 2014, ApJ, 782, 65
Tanigawa, T., Ohtsuki, K., & Machida, M. N. 2012, ApJ, 747, 47
Tanigawa, T., & Tanaka, H. 2016, ApJ, 823, 48
Urpin, V., & Brandenburg, A. 1998, MNRAS, 294, 399
Yang, C.-C., & Menou, K. 2010, MNRAS, 402, 2436
Zhang, K., Blake, G. A., & Bergin, E. A. 2015, ApJL, 806, L7
Zhu, Z., Nelson, R. P., Dong, R., Espaillat, C., & Hartmann, L. 2012, ApJ, 755, 6
Zhu, Z., Nelson, R. P., Hartmann, L., Espaillat, C., & Calvet, N. 2011, ApJ, 729, 47
Zhu, Z., Stone, J. M., Rafikov, R. R., & Bai, X.-n. 2014, ApJ, 785, 122